Nanoscale

PAPER

View Article Online
View Journal | View Issue

Cite this: *Nanoscale*, 2025, **17**, 18690

Differentiating α-synuclein aggregates using charge-sensitive gold nanoclusters†

Harpreet Kaur,[a] Arpit Tyagi,[b,c] Ishani Sharma,[a] Deepak Sharma *[b,c] and Sharmistha Sinha *[a,c]

Received 27th February 2025,
Accepted 3rd July 2025

DOI: 10.1039/d5nr00887e

rsc.li/nanoscale

The accumulation of α-synuclein (α-syn) aggregates in the brain is associated with Parkinson's disease, making it a promising biomarker for understanding the disease's pathogenesis. Distinguishing between oligomeric forms of amyloidogenic proteins is crucial, as their toxicity depends on conformation. This study leverages surface charge differences to distinguish α-syn monomers from amyloids. We employed label-free gold nanoclusters (AuNCs) with distinct surface charges to differentiate between wild-type and mutant [A30P]-α-Syn based on their charge characteristics. Fluorescence spectroscopy and electrochemical measurements were performed to evaluate the sensitivity and interaction mechanisms. Our results show that Pro-AuNCs exhibit greater sensitivity towards monomeric forms of both wild-type and mutant α-Syn, while His-AuNCs are more sensitive to amyloid forms. Impedance spectroscopy shows a detection limit in the picomolar range (pM), which is twice as sensitive as fluorescence measurements. Cell culture studies further validate our *in vitro* findings, demonstrating the effective specificity of AuNCs for detecting different conformations of α-syn. Overall, our results indicate that this probe can successfully identify aggregated and monomeric forms of α-syn, suggesting its potential for developing sensors aimed at understanding the etiology of Parkinson's disease.

Introduction

Conformational changes in proteins, triggered by not only various intracellular or extracellular stimuli but also alterations in physicochemical properties, such as surface charge and hydrophobicity, are crucial for protein function and cellular communication.[1] In particular, variations in surface charge influence protein stability, localization, and interactions, which are essential for protein function within the complex cellular environment.[2,3] A significant example of this is amyloidogenic aggregation, linked to neurodegenerative diseases such as Alzheimer's and Parkinson's.[4,5] During amyloid formation, proteins transition from soluble monomers to oligomers, protofibrils, and mature fibrils.[6,7] Each stage is marked by distinct changes in the protein's surface charge distribution, which affects its interactions with surrounding molecules, such as ions, membranes, and other proteins.[8,9] These charge variations influence aggregation pathways, stability, and toxicity, ultimately impacting the pathogenic potential of aggregates by modifying their affinity for cellular components.[10,11]

We hypothesize that surface charge differences can be exploited to develop sensors capable of selectively detecting different aggregation states, including monomers, oligomers, and fibrils. In this study, we focus on α-synuclein (α-syn), a presynaptic protein implicated in Parkinson's disease (PD), which undergoes amyloid aggregation associated with the formation of Lewy bodies and fibrillar inclusions in dopaminergic neurons.[12,13] The structure of α-syn includes an N-terminal tail, a hydrophobic core, and an acidic C-terminal tail, contributing to its overall negative charge at physiological pH.[14,15] Familial PD mutations, such as A30P, E46K, and A53T, further alter α-Syn's aggregation propensity, leading to toxic protofibrils that disrupt cellular homeostasis and drive neurodegeneration.[16–18]

Electrostatic interactions critically influence the conformational transitions of α-syn from monomer to fibril, highlighting the potential for charge-based detection strategies.[19] Distinct zeta (ζ) potentials between monomeric and aggregated α-syn species present an opportunity for selective detection based on surface charge differentials. Although antibody-based assays and fluorescent probes have been explored, they frequently suffer from limited specificity, high cost, and challenges in clinical translation. Advanced techniques such as spectroscopy, capillary electrophoresis and mass spectrometry

[a]*Institute of Nano Science and Technology, Knowledge City, Sector 81, Mohali, Punjab 140306, India. E-mail: sinhas@inst.ac.in*
[b]*CSIR-Institute of Microbial Technology, Sector 39A, Chandigarh 160036, India*
[c]*Academy of Scientific & Innovative Research (AcSIR), Ghaziabad, India*
† Electronic supplementary information (ESI) available. See DOI: https://doi.org/10.1039/d5nr00887e

offer high sensitivity but are resource-intensive and require specialized instrumentation, underscoring the need for simple, precise, and label-free small-molecule probes.[20–23] While extensive literature studies have characterized the structural differences of α-syn across its aggregation pathway, few approaches effectively discriminate these conformations in a conformation-specific manner. Here, we propose a charge-based strategy to probe distinct α-syn conformers by exploiting differences in surface electrostatics.

Gold nanoclusters (AuNCs), owing to their size-tunable luminescence, chemical stability, and cost-effectiveness, have emerged as promising sensing platforms.[24–27] In this study, we functionalize AuNCs with amino acid coatings to modulate their surface charge and enhance binding selectivity. This strategy enables the development of novel optical and electrochemical sensors capable of distinguishing α-syn aggregates from monomers, offering a label-free, cost-efficient diagnostic tool.

Results

Aggregation of α-Syn variants

In this study, we used two variants of α-Syn, wild-type (WT) and mutant [A30P]-α-Syn, both implicated in PD pathogenesis. The proteins were overexpressed and purified, with purity confirmed *via* SDS-PAGE (Fig. 1a). The hydrodynamic diameters of WT and [A30P]-α-Syn were measured and found to be in the range of 7–10 nm (Fig. 1b), with the corresponding autocorrelation curves exhibiting a smooth, single exponential decay, indicating a monodisperse population for both wild-type and mutant α-syn (Fig. S1†), consistent with previous reports on monomeric α-Syn.[28] Both proteins were then incubated at 37 °C under stirring for 72 hours, with aliquots taken at regular intervals to monitor time-dependent changes in hydrodynamic size (Fig. 1b) and thioflavin T (ThT) fluorescence (Fig. 1c). Zeta potential measurements revealed net negative charges for the monomers: −10 ± 0.5 mV for WT and −14 ± 0.6 mV for [A30P]-α-Syn at 0 h (Fig. 1d), and after 72 h, a shift towards a neutral zeta potential has been observed (Fig. 1d).

After 72 hours, fibrillar aggregates were observed for both variants, confirmed by ThT fluorescence and transmission electron microscopy (TEM) of the endpoint samples (Fig. 1e). Circular dichroism (CD) spectra further confirmed the structural transition from random coil to β-sheet-rich conformations for both WT and [A30P]-α-Syn (Fig. S2†).

Synthesis and characterization of amino acid-capped gold nanoclusters

Gold nanoclusters (AuNCs) were synthesized using histidine and proline as capping agents to investigate interactions with monomeric and amyloidogenic forms of α-syn. The choice of

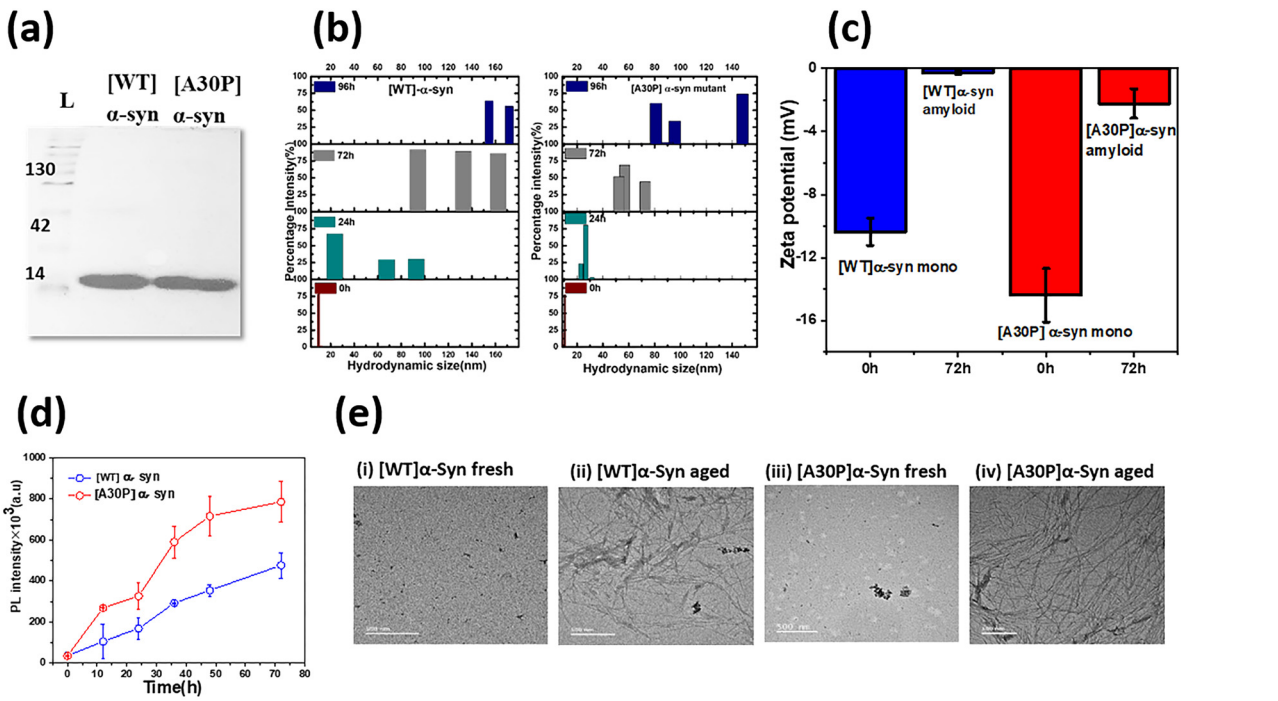

Fig. 1 Characterization of wild-type and mutant α-syn: SDS-PAGE (15%) gel analysis of purified α-Syn and mutant [A30P]-α-Syn (a). The hydrodynamic size of [WT]-α-Syn and [A30P]-α-Syn at different time intervals (0 h, 24 h, 72 h, and 96 h) incubated at 37 °C (b). Zeta potential measurements of wild-type α-Syn and mutant [A30P]-α-Syn on day 0 and after 7 days of incubation (c). Time dependent thioflavin T (ThT) fluorescence intensity, indicating amyloid fibril formation, for wild-type α-Syn and [A30P]-α-Syn for 72 h of incubation at 37 °C (d). Transmission electron microscopy images illustrating the morphological differences in wild type α-Syn and mutant [A30P]-α-Syn monomer and amyloid samples (72 h incubated samples), respectively (e).

amino acids was based on their reducing capabilities, attributed to the imidazole group in histidine and the heterocyclic amine group in proline.[29,30] Under UV illumination, Pro-AuNCs exhibit blue luminescence, while His-AuNCs show bluish-green fluorescence (Fig. 2a). Upon excitation in the range of 350–380 nm, the amino acid-capped gold nanoclusters emit maxima at approximately 490 nm for His-AuNCs and 450 nm for Pro-AuNCs (Fig. 2a). Zeta potential measurements show −10 ± 0.5 mV for His-AuNCs and +4 ± 0.45 mV for Pro-AuNCs (Fig. 2b). Dynamic light scattering (DLS) measurements show hydrodynamic diameters of 4.7 ± 0.25 nm for His-AuNCs and 5.1 ± 0.31 nm for Pro-AuNCs (Fig. 2c). TEM images of the AuNCs (Fig. 2d and e) show spherical clusters with average diameters of 4.5 ± 0.5 nm for His-AuNCs and 5.5 ± 0.4 nm for Pro-AuNCs. High-resolution TEM (HRTEM) images further confirm the crystallinity of the samples (Fig. S3a and b†). Next, to analyse the chemical state of gold in the nanoclusters, we employed X-ray photoelectron spectroscopy (XPS), which revealed C(1s), N(1s), and O(1s) core-level emissions, confirming amino acid stabilization of the atomic gold clusters (Fig. S3c†). Both His-AuNCs and Pro-AuNCs exclusively contained Au (0), as indicated by peaks at 87.26 eV and 83.67 eV for His-AuNCs (Fig. S3c and d†) and 87.48 eV and 83.88 eV for Pro-AuNCs (Fig. S3c and e†), corresponding to the Au 4f7/2 and Au 4f5/2 states. The ultrasmall size of the AuNCs resulted in a shift in binding energies to higher levels, consistent with previous reports on size-dependent electronic properties.[31]

His-AuNCs and Pro-AuNCs interact differently with different conformations of α-Syn variants

To explore the precise molecular charge-based interactions between the α-Syn conformers of the mutant and wildtype and nanoparticles, we utilized native PAGE gel electrophoresis. This method allowed us to track shifts in electrophoretic mobility caused by these interactions as the ratio of nanoclusters gradually increased. We examined the interactions of monomeric wild-type and mutant [A30P]-α-Syn with Pro- and His-capped gold nanoclusters. We observed that the protein–nanocluster complexes showed reduced mobility on the gel due to their higher molecular weight compared to the individual proteins or nanoclusters. When Pro-AuNCs were incubated with monomeric wild-type and mutant [A30P]-α-Syn at increasing ratios (1 : 1, 1 : 3, 1 : 10, and 1 : 30), reduced electrophoretic mobility was observed, indicating the formation of stable protein–nanocluster complexes (Fig. 3a and b). This suggests a strong affinity between Pro-AuNCs and the monomeric forms, in contrast to the behaviour observed with fibrillar forms of α-Syn (Fig. S4a and b†). In contrast, incubating His-AuNCs with monomeric wild-type and mutant proteins, even at a high molar ratio of 1 : 50, resulted in no significant shift in protein bands, indicating minimal interactions between His-AuNCs and the monomeric proteins (Fig. 3c and d). However, a notable shift in band position was observed for fibrillar forms of α-Syn, suggesting an interaction between His-AuNCs and these conformations (Fig. S4c and d†).

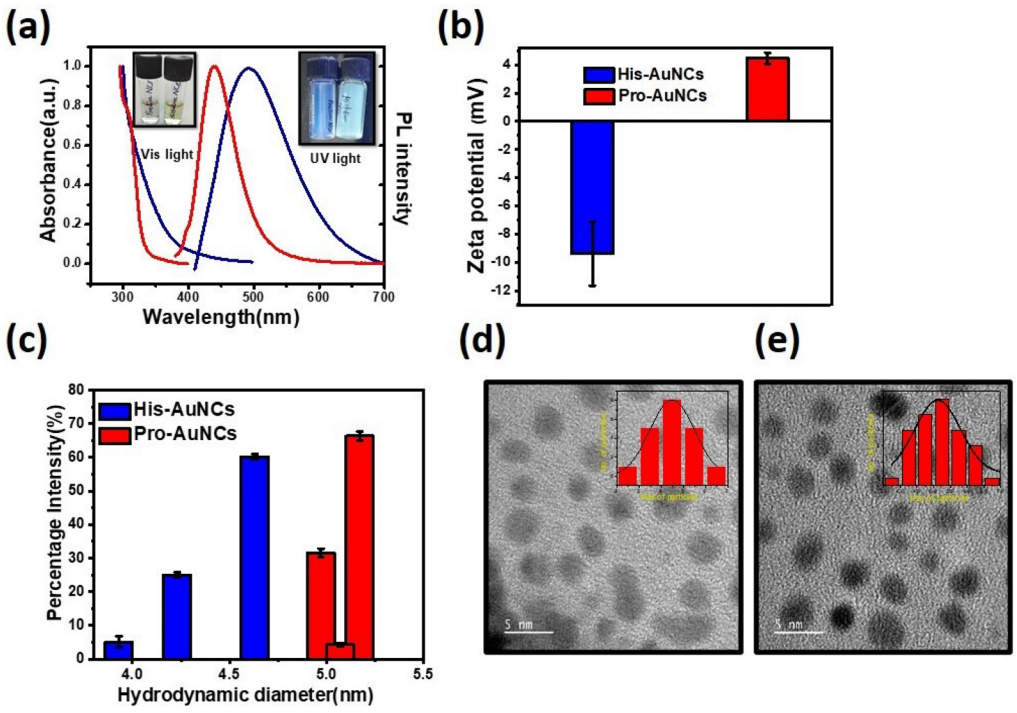

Fig. 2 Characterization of amino acid-capped gold nanoclusters (AuNCs): UV-Vis absorption and fluorescence spectra of His-AuNCs and Pro-AuNCs (a). Zeta potential measurements for His-AuNCs (wine) and Pro-AuNCs (navy blue) (b). Hydrodynamic diameter distribution of His-AuNCs (cyan) and Pro-AuNCs (blue) (c). TEM images of His-AuNCs show that the average particle size is 4.5 nm (d). TEM images of Pro-AuNCs show that the average particle size is 5.5 nm (e).

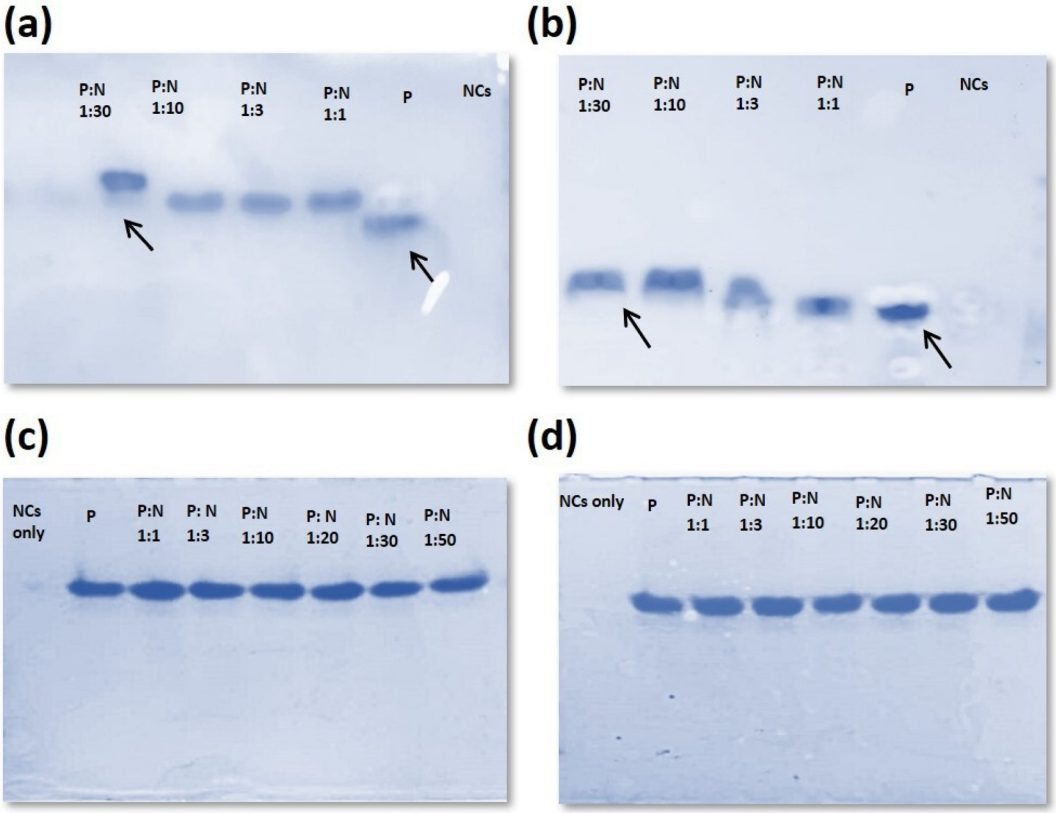

Fig. 3 Interactions of gold nanoclusters with proteins by gel electrophoresis: Native PAGE gel images showing interactions between monomeric wild-type α-Syn and mutant α-Syn ([A30P]-α-Syn) with Pro-AuNCs at various protein-to-nanocluster (P : N) ratios (1 : 1, 1 : 3, 1 : 10, and 1 : 30) (a and b). Native PAGE gel images illustrating interactions of His-AuNCs with monomeric wild-type α-Syn and mutant [A30P]-α-Syn at different P : N ratios (1 : 1, 1 : 3, 1 : 10, 1 : 30, and 1 : 50) (c and d).

These findings support our hypothesis that Pro-AuNCs have a strong interaction with the monomeric forms of wild-type and mutant [A30P]-α-Syn, while His-AuNCs show weaker or negligible interactions. This difference in behavior is likely due to electrostatic interactions: negatively charged monomeric proteins are attracted to positively charged Pro-AuNCs, whereas His-AuNCs, being negatively charged, interact with the positively charged regions of the fibrillar forms.

To further explore these interactions, we conducted steady-state fluorescence spectroscopy.

Fluorescence quenching and binding studies

We began our study by examining the interactions of these proteins, which exhibit different surface charges, with the two types of AuNCs. By titrating His-AuNCs and Pro-AuNCs (1 μM) with increasing concentrations (50 nM to 1 μM) of monomeric and amyloid forms, we observed distinct fluorescence quenching patterns. His-AuNCs exhibited a decrease in fluorescence intensity upon association with amyloid forms (Fig. S5a and c†) but showed minimal change with monomers (Fig. S5b and d†). Conversely, Pro-AuNCs showed a progressive fluorescence decrease with monomers (Fig. S6a and c†) and less change with amyloids (Fig. S6b and d†), suggesting that electrostatic interactions influence these differential behaviours. Stern–Volmer (SV) plots revealed a strong linear relationship between His-AuNCs and amyloids and Pro-AuNCs and monomers.

Using the Stern–Volmer (SV) equation:

$$\frac{F_0}{F} = 1 + K_{SV}\,[\mathrm{NCs}] \quad (1)$$

where K_{SV} indicates the quenching efficiency, we found that His-AuNCs showed higher quenching efficiency for amyloids, while Pro-AuNCs were more efficient with monomers (Fig. 4a and b). The calculated limits of detection (LOD) for His-AuNCs were 64 pM and 80 pM for amyloids, and 138 pM and 320 pM for monomers. Pro-AuNCs exhibited LODs of 66 pM and 81 pM for monomers and 127 pM and 561 pM for amyloids (Table S1†).

These LOD values indicate that our sensitive approach is well-suited for detecting amyloid and monomeric forms of wild-type and mutant proteins using AuNCs, surpassing the previously reported literature where detection limits are typically in the nM range.[32] Additionally, a PE-based sensor has been demonstrated for detecting amyloid forms over monomers based on electrostatic interactions, but with a detection limit only in the μM range.[33] Notably, the Mukherji group has distinguished between α-Syn monomers and fibrils using a localized surface plasmon resonance (LSPR) optical sensing

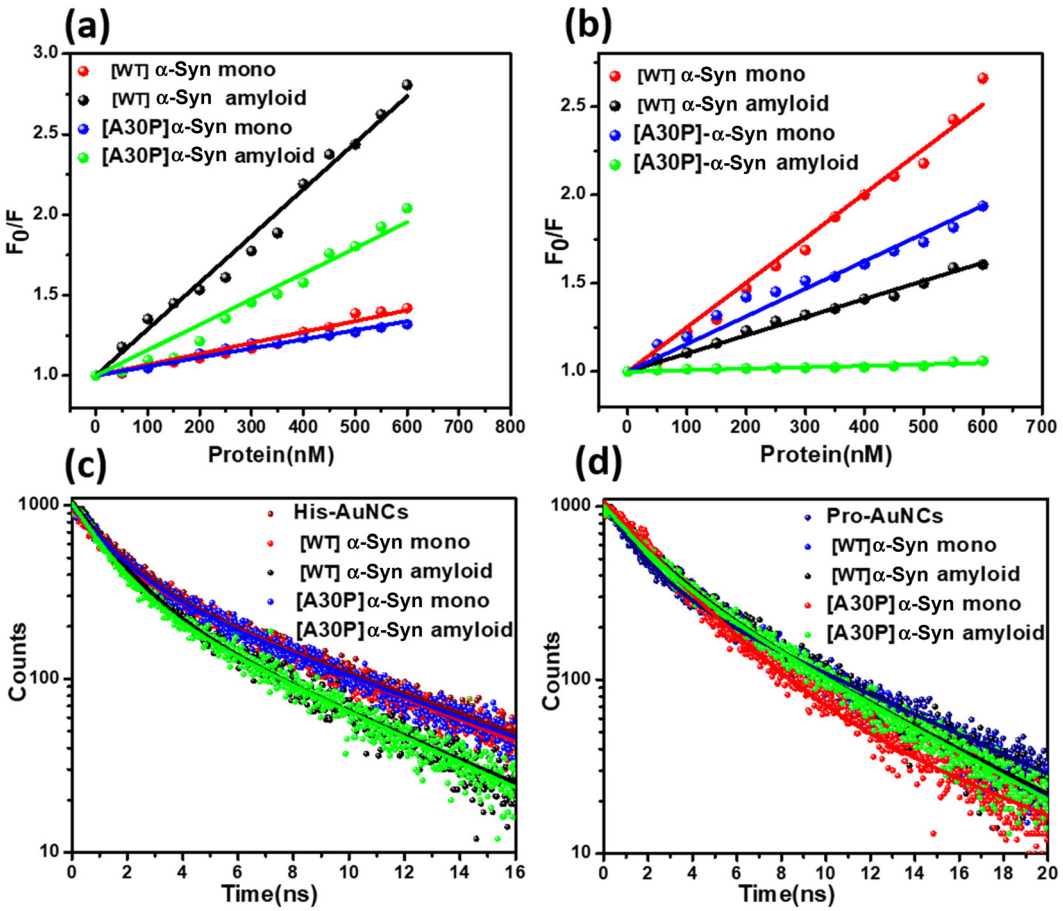

Fig. 4 Fluorescence quenching and lifetime measurement studies: Stern–Volmer plots for His-Au-NCs with varying concentrations (0 nM to 1 μM) of amyloid and monomeric wild type α-Syn and mutant [A30P]-α-Syn (a). Stern–Volmer plots for Pro-Au-NCs with varying concentrations (0 nM to 1 μM) of amyloid and monomeric α-Syn and mutant [A30P]-α-Syn (b). Fluorescence lifetimes of His-Au-NCs in the presence of monomeric and amyloid α-Syn and mutant [A30P]-α-Syn (c). Fluorescence lifetimes of Pro-Au-NCs in the presence of monomeric and amyloid α-Syn and mutant [A30P]-α-Syn (d).

device in the nM range.[34] In contrast, our charge-based optical sensing device exhibits sensitivity in the pM range, making it a powerful tool for differentiating between the amyloid and monomeric forms of proteins during the early stages of disease.

To further investigate the quenching mechanisms, temperature-dependent studies were conducted to distinguish between dynamic and static quenching. Dynamic quenching, which involves collisions between the fluorophore and quencher, increases with temperature, whereas static quenching, due to complex formation, decreases. His-AuNCs showed dynamic quenching with amyloids and static quenching with monomers (Fig. 4a, S7a and Table S2†). Conversely, Pro-AuNCs exhibited dynamic quenching with monomers and static quenching with amyloids (Fig. 4b, S7b and Table S3†). Fluorescence lifetime measurements confirmed these mechanisms. For His-AuNCs, lifetimes decreased significantly upon interaction with amyloids, consistent with dynamic quenching, while they remained unchanged with monomers. For Pro-AuNCs, lifetimes decreased with monomers but were unaffected by amyloids, indicating static quenching (Fig. 4c, d; and Table S4†). Our BLI analysis reveals that both WT and mutant [A30P] monomeric forms exhibit weaker interactions with His-AuNCs compared to their amyloid counterparts (Fig. S8†).

Global fitting of the association and dissociation kinetics for the interactions between His-AuNCs and WT as well as mutant [A30P]-α-Syn monomers yields dissociation constants (K_D) of 1.33 ± 0.154 μM and 5.5 ± 0.02 μM, respectively (Fig. S8a and c†). In contrast, the dissociation constants for the amyloid forms are significantly lower, measuring 5.84 ± 0.1 nM for wild-type and 2.94 ± 0.07 nM for mutant [A30P]-α-Syn (Fig. S8b and d†). In comparison, Pro-AuNCs exhibit a stronger affinity for the monomeric forms of WT and mutant [A30P]-α-Syn than His-AuNCs. After global fitting of the association and dissociation curves for Pro-AuNCs, the dissociation constants are determined to be 131 ± 2.93 nM for the WT monomer and 0.64 ± 0.01 μM for the mutant [A30P] monomer (Fig. S8e and g†). For the amyloid forms, the K_D values are 4.5 ± 0.62 μM and 32.7 ± 0.07 μM, respectively (Fig. S8f and h†).

These findings are notably consistent with our earlier investigations, strongly supporting our hypothesis. These findings demonstrate that His-AuNCs preferentially associate with amyloid forms, whereas Pro-AuNCs target monomeric forms, enabling effective differentiation between protein conformations.

Electrochemical sensing and selectivity studies

We employed cyclic voltammetry (CV) and electrochemical impedance spectroscopy (EIS) to evaluate opposing charge gold nanoclusters (His-AuNCs and Pro-AuNCs) as electroanalytical sensing probes for identifying monomeric and amyloid forms of wild-type (WT) and mutant [A30P]-α-Syn. The nanoclusters were drop-cast onto the electrode surface, and their interactions with varying protein concentrations (0 to 100 pM) were analysed in KCl buffer. The CVs for Nafion/GCE and Nafion/AuNCs/GCE reveal that the cyclic voltammetric response of GCE/His-AuNCs and GCE/Pro-AuNCs increases with the concentration of both monomeric and amyloid proteins (Fig. S9–12†). Notably, the peak current change is less pronounced for monomeric proteins on GCE/His-AuNCs (Fig. S10†), while GCE/Pro-AuNCs show diminished current changes with increasing amyloid concentrations (Fig. S12†). EIS further characterizes the molecular interactions on the electrode surface. For GCE/His-AuNCs, the charge transfer resistance (R_{ct}) increases significantly with amyloid concentrations, indicating reduced ion diffusion at the electrode interface (Fig. S9b and 9e†). Similarly, R_{ct} rises for GCE/Pro-AuNCs with increasing concentrations of monomeric proteins (Fig. 5a, b and S11†). A linear relationship between ΔR and protein concentrations is observed across the studied range. The limit of detection (LOD) is calculated from the slopes of linear graphs, yielding values of 0.12 pM and 0.14 pM for monomeric WT and mutant [A30P]-α-Syn on GCE/Pro-AuNCs, and 0.16 pM and 0.10 pM for amyloid forms on GCE/His-AuNCs (Fig. 5c and d). His-AuNCs show 5-fold and 8-fold higher sensitivity towards amyloid WT and mutant [A30P]-α-Syn, respectively, compared to their monomeric forms. Conversely, Pro-AuNCs exhibit 5-fold and 10-fold greater sensitivity for monomeric WT and mutant [A30P]-α-Syn compared to amyloid forms. Overall, our sensing approach demonstrates superior limits of detection compared to other electrochemical methods (Table 1). The GCE/Pro-AuNCs and GCE/His-AuNCs sensors exhibit excellent performance for detecting the distinct forms of wild-type and mutant [A30P]-α-Syn.

Additionally, the specificity of the developed sensing system for wild-type and mutant [A30P]-α-Syn is evaluated by comparing it with bovine serum albumin (BSA) under optimized conditions. The measured zeta potential of BSA is −10 mV (Fig. S13†), indicating its negative charge in the monomeric

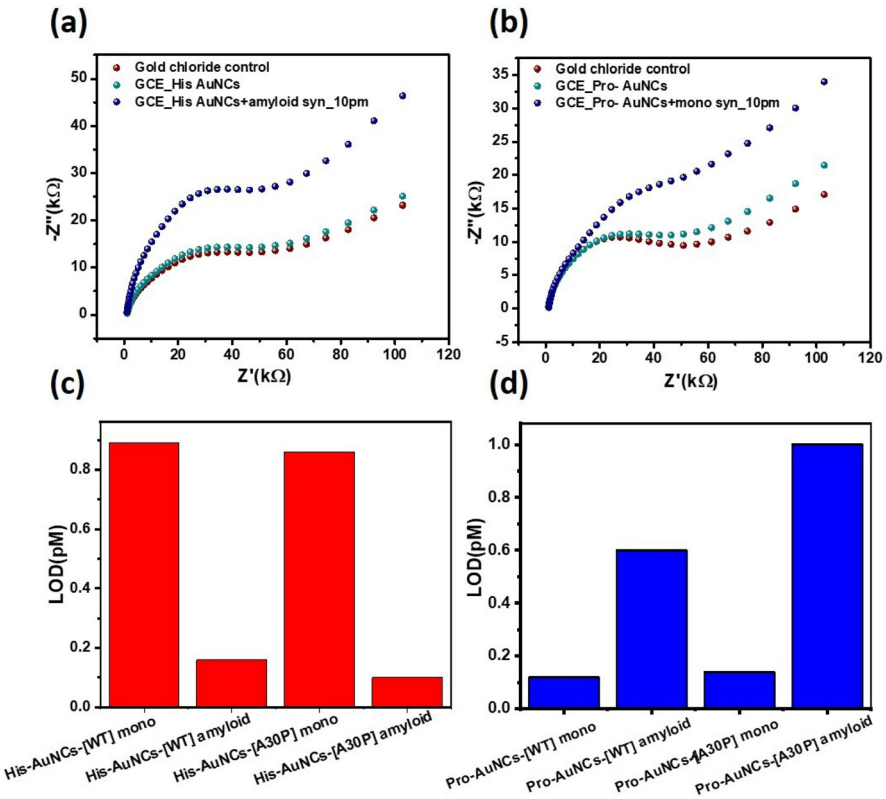

Fig. 5 Impedance measurement studies: Impedance spectra of GCE_His-AuNCs (a) and GCE_Pro-AuNCs (b) in the presence of amyloid and monomeric [WT]-α-Syn, respectively. Limit of detection measurements for His-AuNCs with monomeric and amyloid forms of [WT]-α-Syn and the mutant [A30P]-α-Syn (c). Limit of detection measurements for Pro-AuNCs with monomeric and amyloid forms of [WT]-α-Syn and the mutant [A30P]-α-Syn(d).

Table 1 Comparison of the sensing performance of the developed system with existing systems for α-syn detection

Electrode/materials	Method	LOD	Ref.
DNA aptamer	EIS	1 pM	(Sun *et al.*, 2017)[35]
G4-polyamidoamine dendrimer-encapsulated Au nanoparticles.	CV	1 pM	(An *et al.*, 2012)[36]
Apt/CS/α-Syn oligomer/Exo/TdT/Au	DPV	10 pM	(Taghdisi *et al.*, 2019)[37]
Syn ab/PEG film /EDC-NHS/Au electrode	EIS	21 ± 4 pM	(Xu *et al.*, 2014)[38]
Gold nanoparticle-conjugated aptamer	CV	10 pM	(You *et al.*, 2019)[39]
U-shaped fiber optic/AuNCs	LSPR	70 nM	(Khatri *et al.*, 201)[32]
GCE/His-AuNCs/Pro-AuNCs	CV, EIS	0.1 pM	This work

form. When titrating 1 μM Pro-AuNCs with increasing BSA concentrations (from 50 nM to 1000 nM), no significant changes in fluorescence are observed, suggesting minimal interaction. However, when the concentration of monomeric BSA is increased to 10 μM, a notable increase in fluorescence intensity occurs, indicating interaction at the micromolar level (Fig. S14†). The limit of detection (LOD) calculated from the Stern–Volmer plot is found to be 0.18 μM. To further test selectivity, we generate BSA amyloid by lowering the buffer pH and heating the solution to 65 °C for one hour under saline conditions, which is confirmed using a thioflavin T assay (Fig. S15b†). The zeta potential of the BSA amyloid is measured at −0.81 mV (Fig. S13a†). When titrating His-AuNCs with increasing concentrations of BSA amyloid, no change in fluorescence intensity is observed from 50 nM to 900 nM (Fig. S15a†). However, at 10 μM, there is a significant enhancement in fluorescence, indicating interaction at the micromolar range (Fig. S15b†). The calculated LOD from the slope is 0.133 μM. These results confirm that our sensing system is both sensitive and selective for wild-type α-Syn and mutant [A30P]-α-Syn, distinguishing them from other charged proteins present in the environment.

Detection of [WT]-α-Syn aggregates in cell studies

To assess the impact of nanoclusters on cell viability prior to their use in cell studies, we conducted the MTT assay using SH-SY5Y cells. This assay evaluated the effect of AuNCs (Pro-AuNCs and His-AuNCs) on cell viability across a range of concentrations (0 to 200 μM). The results show that cell viability for both types of AuNCs remains above 80%, up to a concentration of 80 μM (Fig. 6a and b). Consequently, we selected 80 μM as the concentration for further colocalization experiments.

To evaluate the specificity of His-AuNCs and Pro-AuNCs under cellular conditions, we transfected SH-SY5Y cells with the plasmid encoding eGFP-α-Syn. Subsequently, we treated them with preformed α-Syn fibrils.

After 24 hours, the SH-SY5Y cells showed α-syn as both diffused and punctate green. The cells were then incubated with Rhodamine-B-tagged His-AuNCs and Pro-AuNCs (the surface charge checked before use is shown in Fig. S16†) for 30 minutes, after which imaging was carried out to examine the colocalization of AuNCs with the distinct forms of α-Syn. His-AuNCs exhibited colocalization with the fibrillar (punctate) form of α-Syn, as indicated by the merged image shown in Fig. 6c and d. In contrast, Pro-AuNCs showed a significant colocalization with the diffused form of α-syn (diffused EGFP as compared to Rhodamine-B signal). Colocalization coefficients were calculated using Pearson's coefficient (PC) and Manders' overlap coefficients (M1 and M2). M1 indicates the overlap of rhodamine-B with eGFP α-Syn, while M2 indicates the overlap of eGFP-α-syn with Rhodamine-B signal (Fig. 6e and f). These results confirm our *in vitro* findings, demonstrating the specific affinity of AuNCs for different forms of α-Syn.

Discussion

In this study, we present a charge-guided nanosensing strategy employing oppositely charged gold nanoclusters (AuNCs) to discriminate between monomeric and fibrillar forms of wild-type and mutant [A30P]-α-syn, proteins centrally implicated in Parkinson's disease. His-AuNCs and Pro-AuNCs, capped with histidine and proline, respectively, exhibit distinct electrostatic properties and fluorescence profiles. Through steady-state fluorescence spectroscopy, we show that His-AuNCs selectively associate with β-sheet-rich amyloid fibrils, while Pro-AuNCs preferentially bind monomeric forms, with quenching mechanisms governed by temperature-dependent interactions—dynamic for His-AuNCs and amyloids, and static for Pro-AuNCs and monomers. These trends were corroborated by fluorescence lifetime analysis and Stern–Volmer modeling, yielding detection limits (LOD) in the picomolar range (His-AuNCs: 64–80 pM for amyloids; Pro-AuNCs: 66–81 pM for monomers), significantly outperforming previously reported sensors.

Electrochemical impedance spectroscopy (EIS) and cyclic voltammetry (CV) further validated this discrimination. Impedance-based sensing achieved even higher sensitivity, with LODs down to 0.10–0.16 pM, highlighting the synergistic role of electrostatics and nanoconfinement in enhancing surface interaction and signal transduction. Control experiments using bovine serum albumin (BSA) in both monomeric and amyloid forms confirmed the high selectivity of the system toward α-Syn. Cell-based colocalization studies using SH-SY5Y cells transfected with EGFP-tagged α-Syn supported the *in vitro* findings: His-AuNCs co-localized with punctate amyloid structures, while Pro-AuNCs targeted the diffuse monomeric distribution. These results demonstrate the ability of charge-tuned AuNCs to serve as conformer-specific molecular reporters in complex biological settings.

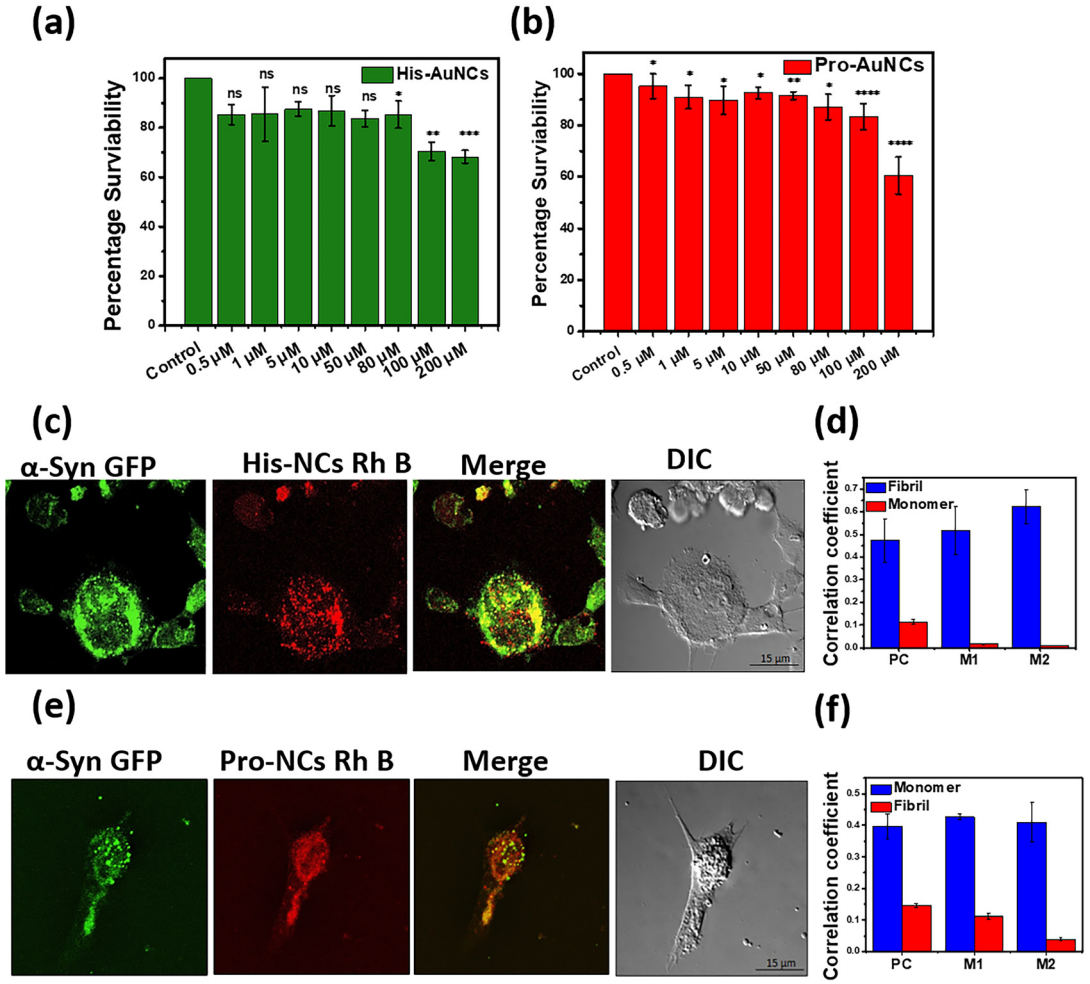

Fig. 6 Cytotoxicity and cellular localization of AuNCs in SH-SY5Y cells: SH-SY5Y cells treated with varying concentrations of (a) Pro-NCs and (b) His-NCs. Cell viability was assessed after 30 minutes of incubation. Results averaged from three independent experiments. Statistical significance: **P* = 0.1, ***P* = 0.01, ****P* = 0.00 1, ns = not significant (one-way ANOVA). Rhodamine-tagged His-AuNCs showing affinity for the punctate (fibril) form, depicted from the merged colocalization of red (rhodamine B) and green (eGFP) channels showing yellow fluorescence from fibrils (c). Correlation coefficient for the punctate EGFP signal relative to rhodamine B (d). Colocalization of Pro-NCs rhodamine B with monomeric α-syn EGFP, as shown from confocal images showing the merged colocalization of the green and red channels (e). Correlation coefficient for the diffuse EGFP signal relative to the rhodamine B signal (f) (scale bar: 15 μm. PC: Pearson's coefficient; M1 & M2: Mander's overlap coefficients).

Conclusion

We have established a sensitive and selective nanosensing framework using oppositely charged AuNCs to distinguish between the pathological and physiological conformers of α-syn. This dual-mode detection system integrates fluorescence and electrochemical modalities, offering sub-picomolar detection and precise structural selectivity. Importantly, the system functions effectively in both purified protein environments and living cells, indicating strong translational potential.

Looking ahead, this platform can be further engineered into wearable or implantable biosensors for real-time monitoring of protein aggregation in neurodegenerative diseases. Its modularity allows extension to other aggregation-prone proteins, opening new avenues for early diagnosis and mechanistic studies of protein misfolding disorders at the nanoscale.

Experimental section

Materials

Hydrogen tetrachloroaurate trihydrate ($HAuCl_4 \cdot 3H_2O$), glycine, Tris HCl, proline, L-histidine, streptomycin sulphate, and EDTA are purchased from Sigma-Aldrich (India). Sodium chloride (NaCl), sodium hydroxide (NaOH), hydrochloric acid (HCl), and ammonium sulphate were obtained from HiMedia. All chemicals were of analytical reagent grade. Ultrapure water (18.2 MΩ cm^{-1}, Millipore) was used to prepare all aqueous solutions. All the chemicals used in this study were commercially available and consumed without any purification.

Expression and purification of [WT]-α-Syn and [A30P]-α-Syn

The purification of recombinantly expressed human [WT]-α-Syn protein and mutant [A30P]-α-Syn was done using a pre-

viously reported protocol.[40] The [WT]-α-Syn containing plasmid was transformed into BL21(DE3). The overnight-grown culture cells were inoculated (1%) into fresh culture media and grown until the optical density reached 0.6–0.8. The cultured cells were induced with 0.8 mM IPTG, followed by incubation at 37 °C for 4 h. Centrifugation was performed at 4000 rpm for 30 minutes to harvest the cultured cells. The pellet obtained was further resuspended in buffer A (10 mM Tris-Cl pH 7.5, 150 mM NaCl, and 1 mM EDTA pH 8.0), followed by incubation at 90 °C for 20 min for lysis of cells. The cell lysate was centrifuged at 12 000 rpm for 20 min to remove the cell debris. The nucleic acids were removed by adding streptomycin sulfate and glacial acetic acid, followed by centrifugation. Furthermore, the protein precipitation was achieved by adding an equal volume of a saturated solution of ammonium sulphate, followed by ethanol precipitation. The finally obtained pellet was dissolved in 10 mM Tris-Cl pH 7.5. The purification protocol for [A30P]-α-Syn was the same as that for wild-type α-Syn. The concentrations of purified [WT]-α-Syn and [A30P]-α-Syn were calculated by UV–visible spectroscopy based on tyrosine absorbance at 274 nm using a molar extinction coefficient of 5600 M^{-1} cm^{-1} (ref. 41). The purity of the proteins was checked by SDS PAGE gel electrophoresis.

Thioflavin T fluorescence assay

Thioflavin T binding studies were performed to check the formation of amyloid from monomeric forms of [WT]-α-Syn and mutant [A30P]-α-Syn. For this, the protein samples (100 μM) were incubated at 37 °C under stirring for 7 days. The freshly prepared ThT (10 μM) was added to the protein samples and the change in fluorescence intensity was recorded at 490 nm with excitation at 440 nm.

Transmission electron microscopy (TEM)

TEM was used to examine the morphology of proteins [WT] and mutant [A30P]-α-Syn in their monomeric and amyloid forms. The protein samples (10 μl of 10 μM) were allowed to absorb onto formvar-coated grids (300 mesh size) for 2 minutes in both the initial (monomeric) and final amyloid forms (7 days incubated samples). Filter paper was used to wipe away excess samples before the grids were stained for 30 seconds with 1% uranyl acetate, washed with Milli-Q water, and dried in a desiccator for 24 hours at room temperature. The JEM 2100 TEM (JEOL, USA) was used for TEM imaging and was run at 120 kV.

Circular dichroism spectroscopy

Circular dichroism was performed to check the secondary structural changes due to the formation of amyloid fibrils from the monomeric forms of [WT]-α-Syn and mutant [A30P]-α-Syn. For this, the samples were incubated at 37 °C under shaking conditions for 7 days. Circular dichroism spectra of the protein samples (at a concentration of 10 μM) were recorded at day 0 and day 7 using a circular dichroism (CD) spectrophotometer (Jasco J-1500) at a wavelength range of 190–250 nm.

Dynamic light scattering studies

The hydrodynamic size and surface charge of [WT]-α-syn and mutant [A30P]-α-syn were measured using a ZetaSizer Nano ZSP (Malvern Instruments).

Preparation of fluorescent histidine and proline capped AuNCs

Histidine- and proline-capped gold nanoclusters were synthesized according to an earlier reported method with minor modifications.[42,43] Firstly, the glassware was cleaned carefully with aqua regia (HNO_3/HCl, 1 : 3 ratio), followed by rinsing with double-distilled water. An aqueous solution of $HAuCl_4$ (2 mL, 5 mM) was prepared and added to aqueous solutions of histidine and proline (2 mL, 50 μM), respectively, in two small separate glass vials. The vial containing histidine and $HAuCl_4$ solution was stirred initially for 1 h at room temperature and then placed in the dark for the formation of gold nanocluster solution for 12 h. The color of the mixture changed from yellow to pale yellow, suggesting the formation of His-AuNCs. The proline mixture was stirred for 10 min at room temperature, followed by increasing the temperature up to 90 °C for 10 min to proceed with the reaction. The solution mixture changed color from canary yellow to light brown, followed by cooling down to room temperature. The color change indicated the formation of proline-capped gold nanoclusters. The gold nanoclusters were stored at 4 °C for further use.

Characterization of amino acid capped gold nanoclusters

The UV–visible spectra of the amino acid-capped gold nanoclusters were recorded either using a double beam UV-Vis spectrophotometer (Agilent Technologies, Cary 60 UV-Vis) or a multimode microplate reader (BioTek Eon™). The absorbance spectra were recorded in the range of 250 to 600 nm. The formation of the fluorescent gold nanoclusters was analysed using a fluorescence spectrofluorometer (FS5, Module SC-5, standard cuvette holder from Edinburgh Instruments, UK). The His-AuNCs were excited at 380 nm and the fluorescence emission range was set as 400 to 700 nm. The Pro-AuNCs were excited at 350 nm and the fluorescence emission scan range was set as 380 to 700 nm. The excitation and emission bandwidths were set to 3 nm, and each spectrum was the average of three scans. The size distribution of each nanocluster and zeta potential were measured on a Zetasizer Nano ZSP (Malvern Instruments). The elemental composition and the oxidation state of gold were analysed using X-ray photoelectron spectroscopy (XPS, Thermo Fisher, ESCALAB 250Xi) with a monochromatic Al Kα X-ray source. Transmission electron microscopy (TEM) was used to examine the morphology of His-AuNCs and Pro-AuNCs. 10 μl of 0.5 mg ml^{-1} nanoclusters was drop-cast onto carbon coated TEM grids, followed by washing with Milli-Q water and drying in a desiccator for 24 hours at room temperature. A JEM 2100 TEM (JEOL, USA) was used for TEM imaging at 200 kV.

Interactions of nanomaterials with monomeric proteins by native PAGE

Native PAGE was employed to visualize the interaction of two kinds of AuNCs with a monomeric form of proteins (wild type

and mutant) to get an idea about the kind of interaction, if any. The strong interactions could be seen by gel electrophoresis. In native PAGE, we used 4–20% gradient gel, which does not have stacking gel. The amino acid capped nanoclusters and proteins ([WT]-α-Syn and the mutant [A30P]-α-Syn) were mixed at different ratios and incubated for 1 h at room temperature, followed by loading onto sample wells of gels. Native gel electrophoresis was performed using Tris/glycine running buffer (25 mM Tris pH 8.8, 192 mM glycine). The loading dye of native gel included 1 mg mL^{-1} bromophenol blue, 20 mM Tris pH 8, and 50% (v/v) glycerol. The gels were run at 100 V for 4 h at room temperature and stained with Coomassie Brilliant Blue R-250.

Fluorescence quenching studies

Steady-state fluorescence spectra of gold nanoclusters (1 μM) with different concentrations of wild type [WT]-α-Syn and mutant [A30P]-α-Syn proteins in their monomeric and amyloid forms were recorded on a spectrofluorometer (FS5, Module SC-5, standard cuvette holder from Edinburgh Instruments, UK). The excitation wavelengths of histidine and proline-capped nanoclusters were set as 380 nm and 350 nm, respectively, and the fluorescence emission range was set as 400–700 nm. The bandwidths for the excitation and emission silts were both set as 3.0 nm and each spectrum is the average of three scans. The concentrations of both types of amino-capped gold nanoclusters were maintained at 1 μM and [WT]-α-Syn and mutant [A30P]-α-Syn in their monomeric and amyloid forms were added to the nanocluster solution, resulting in a different extent of fluorescence quenching. For checking the selectivity of the system, we chose the globular protein BSA as a control due to its large abundance and negative charge. BSA powder was dissolved in 5 mM phosphate buffer (pH 7.0) to prepare a stock solution of 1 mM concentration. The stock solution was further diluted to lower concentrations. To aggregate BSA, 1 mM stock solution was further diluted tenfold using 50 mM glycine-HCl buffer (pH 3) to make a final concentration of 100 μM. The protein sample was incubated with 50 mM NaCl at an increased temperature of 65 °C for 1 h without agitation.

Temperature-dependent fluorescence spectroscopic studies

Fluorescence tests were conducted at different temperatures to distinguish static quenching from dynamic quenching by the different temperature effects (294 K, 298 K, 303 K, and 308 K). The quenching constant was obtained at each temperature by employing the Stern–Volmer equation to calculate the quenching constant:

$$(F_0/F) = 1 + K_{SV}[Q]$$

where F_0 and F are the fluorescence intensities of nanoclusters in the absence and presence of the proteins, respectively, and [Q] is the concentration of proteins. K_{SV} is the Stern–Volmer constant that is used to estimate the quenching efficiency.

Fluorescence lifetime decay studies

Lifetime measurements were performed using the time-correlated single photon counting system (TCSPC, Horiba Jobin Yuvon IBH, UK) with a fast response red-sensitive PMT detector (Hamamatsu Photonics, Japan). The fluorescence quenching of amino acid-capped gold nanoclusters in the presence of monomeric and amyloidogenic forms of [WT]-α-Syn and their mutant [A30P]-α-Syn was determined by using a time-resolved fluorescence decay study. Fluorescence decay curves could be fitted by a single exponential function by using the following equation:

$$y = A_1 \times \exp(-x/t_1) + y_0$$

where A_1 is the value of amplitude, t_1 is the time and y_0 is the offset value. The fluorescence lifetime decay was determined by exciting the histidine-capped nanoclusters and proline-capped gold nanoclusters at 380 nm and 350 nm, respectively.

Biolayer interferometry studies

Biolayer interferometry measurements were used to determine the binding affinities of His-AuNCs and Pro-AuNCs towards wild-type and mutant α-Syn monomers and amyloids (ForteBio Octet K2, Molecular Devices, USA). A solution containing 40 mM 1-ethyl-3-(3-dimethyl aminopropyl) carbodiimide (EDC) and 20 mM *N*-hydroxy succinimide (NHS) combined in a 2 : 1 molar ratio was used to activate amine reactive second generation (AR2G) biosensors. On the activated sensor, 10 μM of either the wild-type or mutant [A30P]-α-Syn (monomer or amyloid form) was loaded. To hide the unbound sites after loading, the sensors were submerged in ethanol amine (pH 8.0). After that, to allow for association, the AR2G sensors were submerged in solutions of wild-type and mutant [A30P]-α-Syn monomer or amyloid forms in PBS pH 7.4 at various concentrations ranging from 1 μM to 10 μM for 500 s. Dissociation was monitored by immersing the biosensor in 10 mM PBS pH 7.4 for 500 s. The sensors were regenerated in 2 M NaCl. The association and dissociation kinetics were globally fitted using the Data Analyzer HT 9.0.0.33 software provided with the Octet K2 instrument.

Electrochemical measurements

The glassy carbon electrode (GCE) was firstly polished with alumina slurries sequentially and then rinsed with DI water, followed by cleaning of electrodes using an ultrasonic bath for 5 minutes in acetone, ethanol, and water. Then, GCEs were dried at room temperature. 5 mg ml^{-1} lyophilized AuNCs were suspended in 1 ml of ethanol, followed by ultrasonication of the suspension for 30 min. Afterward, 8 μl of AuNCs/ethanol suspension was dropcast onto the cleaned glassy carbon electrodes and the solvent was allowed to evaporate. After solvent evaporation, 5 μl of Nafion solution (1% Nafion in ethanol) was dropcast onto the top of the AuNC suspension and dried in air to entrap the clusters on the surface of the GCE. Each electrode was submerged in DI water before use to allow the Nafion membrane to swell. Cyclic voltammetry (CV) and impedance measurements were performed in a conventional three-electrode PGSTAT-30 electrochemical workstation (AutoLab). Electrochemical studies were performed in the conventional three-electrode system, consisting of a working electrode

(GCE), an Ag/AgCl reference electrode, and a platinum counter electrode. CV and impedance measurements were optimized in PBS (pH 7) containing 0.1 M KCl using an electrochemical workstation. In CV, the potential range was from −0.1 to 0.8 V at a scan rate of 10 mV s^{-1}. Electrochemical impedance spectroscopy studies were performed at a potential of 0.25 V in the frequency range of 0.01–500 kHz. For signal amplified detection, the gold nanocluster covered GCE was incubated with the α-Syn samples (WT and mutant), followed by washing with water. After that, the electrode was placed in the electrolyte solution (PBS pH 7, 0.1 M KCl) for cyclic voltammetry and impedance measurements.

Immobilization of rhodamine B on the surface of gold nanoclusters

Rhodamine B was immobilized on the surface of AuNCs as reported earlier. Briefly, 1 ml of AuNCs (50 mM) was mixed with 1 μM of rhodamine B solution (10 μM) and allowed to incubate overnight at 4 °C under stirring conditions. The free dye was removed by dialyzing the incubated solution in water. Afterward, the fluorescence intensity of AuNCs-Rh was monitored by exciting the solution at 546 nm and the emission spectra were recorded on a spectrofluorometer. The zeta potential was also measured after labelling of AuNCs with rhodamine B on a ZetaSizer Nano ZSP.

Cell culture studies

SH-SY5Y cells (CRL-2266™, ATCC) were transfected with the eGFP-α-syn-WT plasmid (Plasmid-40822, Addgene) using the Lipofectamine 2000 transfection reagent (Thermo Fisher Scientific, Darmstadt, Germany). The cells were cultured in advanced DMEM (Gibco) supplemented with 10% fetal bovine serum (Thermo Fisher Scientific, Darmstadt, Germany) and penicillin/streptomycin (100 units per mL, 100 μg mL^{-1}; Thermo Fisher Scientific, Darmstadt, Germany). For the experiment, 0.3×10^6 cells were seeded in a 35 mm Petri dish containing a coverslip and incubated under a humidified atmosphere with 5% CO_2 at 37 °C. After 8 h, the cells were exposed to 3 μM pre-formed fibrils (PFF). After 24 h, the cells were incubated with His and Pro-NCs (rhodamine-tagged) for 30 minutes for confocal microscopy studies.

Cytotoxicity assay

The cellular viability was examined using the MTT assay (3-(4,5-dimethylthiazolyl-2)-2,5-diphenyltetrazolium bromide (Cat. no. M5655, Sigma)). This assay evaluates the proliferation rate of cells, as only viable cells can reduce MTT to formazan crystals through the action of mitochondrial dehydrogenase enzymes. For the assay, SH-SY5Y cells were seeded at a density of 1.6×10^5 and were treated with varying concentrations of AuNCs (ranging from 0 to 200 μM) for 24 h. MTT was added at a working concentration of 0.5 mg ml^{-1} in PBS (pH −07). Following 4 h of incubation, absolute DMSO (100 μl) was added to each well to dissolve formazan crystals and the absorbance was obtained at 570 nm. One-way ANOVA was used to calculate statistical significance.

Colocalization of AuNCs with the monomer and fibril forms of [WT]-α-Syn by confocal microscopy

eGFP-α-Syn-WT plasmid-transfected cells were treated with preformed fibrils (PFF) for 24 hours. The cells without PFF treatment were used as controls. Cells were incubated with gold AuNCs for 30 minutes under a humidified atmosphere with 5% CO_2 at 37 °C. The cells were washed three times with PBS (pH −07) and fixed in 4% paraformaldehyde for 10 minutes. Subsequently, confocal microscopy was carried out, with rhodamine B excited at 546 nm (emission peak at 567 nm) and eGFP excited at 488 nm (emission peak at 509 nm). Images were analyzed using the ImageJ Fiji software. Colocalization analysis of eGFP-α-syn and rhodamine-tagged NCs was performed using the JACoP Plugin in ImageJ. Correlation coefficients were calculated as reported earlier.[44]

Author contributions

Harpreet Kaur: experimental design and execution, methodology, data analysis, manuscript drafting, and editing. Arpit Tyagi: cell culture experiment execution and analysis. Ishani Sharma: experiments, manuscript drafting and editing. Deepak Sharma and Sharmistha Sinha: conceptualization, design, supervision, experimental discussion, data analysis, manuscript writing, and editing.

Conflicts of interest

There are no conflicts of interest to declare.

Data availability

Part of the data supporting the findings of the manuscript is presented in the ESI.† Additional data if required will be available on request.

Acknowledgements

We acknowledge INST for the central instrument facilities. HK acknowledges INST for the fellowship IS acknowledges UGC, India and AT acknowledges the CSIR, India for the fellowship. DS acknowledges funding support from the ICMR grant (IIRPIG/12/2023-0001050). The authors acknowledge members of the laboratory for helpful discussions. The authors acknowledge Mr S. M. Rose for critically reading the manuscript.

References

1 L. Schweizer and L. Mueller, in *Biased Signaling in Physiology, Pharmacology and Therapeutics*, ed. B. J. Arey, Academic Press, San Diego, 2014, pp. 209–249.
2 S. Qin and H.-X. Zhou, *Biopolymers*, 2007, **86**, 112–118.

3 F. B. Sheinerman, R. Norel and B. Honig, *Curr. Opin. Struct. Biol.*, 2000, **10**, 153–159.
4 B. S. Shastry, *Neurochem. Int.*, 2003, **43**, 1–7.
5 G. B. Irvine, O. M. El-Agnaf, G. M. Shankar and D. M. Walsh, *Mol. Med.*, 2008, **14**, 451–464.
6 D. J. Selkoe, *Nat. Cell Biol.*, 2004, **6**, 1054–1061.
7 R. Wetzel, S. Shivaprasad and A. D. Williams, *Biochemistry*, 2007, **46**, 1–10.
8 M. Bucciantini, E. Giannoni, F. Chiti, F. Baroni, L. Formigli, J. Zurdo, N. Taddei, G. Ramponi, C. M. Dobson and M. Stefani, *Nature*, 2002, **416**, 507–511.
9 P. K. J. Kinnunen, *Open Biol. J.*, 2009, **2**, 163–175.
10 C. Haass and D. J. Selkoe, *Nat. Rev. Mol. Cell Biol.*, 2007, **8**, 101–112.
11 S. Lee, M. C. Choi, K. Al Adem, S. Lukman and T.-Y. Kim, *Sci. Rep.*, 2020, **10**, 5120.
12 W. J. Schulz-Schaeffer, *Acta Neuropathol.*, 2010, **120**, 131–143.
13 V. M.-Y. Lee and J. Q. Trojanowski, *Neuron*, 2006, **52**, 33–38.
14 M. C. Bennett, *Pharmacol. Ther.*, 2005, **105**, 311–331.
15 V. N. Uversky, *Curr. Protein Pept. Sci.*, 2008, **9**, 507–540.
16 K. A. Conway, S.-J. Lee, J.-C. Rochet, T. T. Ding, R. E. Williamson and P. T. Lansbury, *Proc. Natl. Acad. Sci. U. S. A.*, 2000, **97**, 571–576.
17 K. Ono, T. Ikeda, J. Takasaki and M. Yamada, *Neurobiol. Dis.*, 2011, **43**, 715–724.
18 S. Sahay, D. Ghosh, S. Dwivedi, A. Anoop, G. M. Mohite, M. Kombrabail, G. Krishnamoorthy and S. K. Maji, *J. Biol. Chem.*, 2015, **290**, 7804–7822.
19 S. Mukherjee, A. Sakunthala, L. Gadhe, M. Poudyal, A. S. Sawner, P. Kadu and S. K. Maji, *J. Mol. Biol.*, 2023, **435**, 167713.
20 P. Verwilst, H. S. Kim, S. Kim, C. Kang and J. S. Kim, *Chem. Soc. Rev.*, 2018, **47**, 2249–2265.
21 H. Mischak, J. J. Coon, J. Novak, E. M. Weissinger, J. Schanstra and A. F. Dominiczak, *Mass Spectrom. Rev.*, 2009, **28**, 703–724.
22 S. Thirunavukkuarasu, E. A. Jares-Erijman and T. M. Jovin, *J. Mol. Biol.*, 2008, **378**, 1064–1073.
23 R. R. Abzalimov, A. K. Frimpong and I. A. Kaltashov, in *Intrinsically Disordered Protein Analysis: Volume 2, Methods and Experimental Tools*, ed. V. N. Uversky and A. K. Dunker, Springer, New York, NY, 2012, pp. 365–373.
24 N. Jaiswal, N. Mahata and N. Chanda, *Nanoscale*, 2025, **17**, 11191–11220.
25 K. Tan, H. Ma, X. Mu, Z. Wang, Q. Wang, H. Wang and X.-D. Zhang, *Anal. Bioanal. Chem.*, 2024, **416**, 5871–5891.
26 Y. Cong, J. Liu, J. Zhang, J. Wang, X. Wang and L. Li, *ACS Appl. Bio Mater.*, 2024, **7**, 2695–2703.
27 B. Casteleiro, J. M. G. Martinho and J. P. S. Farinha, *Nanoscale*, 2021, **13**, 17199–17217.
28 S. W. Chen, S. Drakulic, E. Deas, M. Ouberai, F. A. Aprile, R. Arranz, S. Ness, C. Roodveldt, T. Guilliams, E. J. De-Genst, D. Klenerman, N. W. Wood, T. P. J. Knowles, C. Alfonso, G. Rivas, A. Y. Abramov, J. M. Valpuesta, C. M. Dobson and N. Cremades, *Proc. Natl. Acad. Sci. U. S. A.*, 2015, **112**, E1994–E2003.
29 F. Gong, R. Peng, Q. Wu, H. Zhang, Y. Luo and Q. Cui, *Colloids Surf., A*, 2022, **641**, 128608.
30 X. Mu, L. Qi, P. Dong, J. Qiao, J. Hou, Z. Nie and H. Ma, *Biosens. Bioelectron.*, 2013, **49**, 249–255.
31 D. M. Chevrier, A. Chatt and P. Zhang, *J. Nanophotonics*, 2012, **6**, 064504.
32 A. Khatri, N. Punjabi, D. Ghosh, S. K. Maji and S. Mukherji, *Sens. Actuators, B*, 2018, **255**, 692–700.
33 A. M. Fanni, F. A. Monge, C.-Y. Lin, A. Thapa, K. Bhaskar, D. G. Whitten and E. Y. Chi, *ACS Chem. Neurosci.*, 2019, **10**, 1813–1825.
34 A. Khatri, N. Punjabi, D. Ghosh, S. K. Maji and S. Mukherji, *Sens. Actuators, B*, 2018, **255**, 692–700.
35 K. Sun, N. Xia, L. Zhao, K. Liu, W. Hou and L. Liu, *Sens. Actuators, B*, 2017, **245**, 87–94.
36 Y. An, X. Jiang, W. Bi, H. Chen, L. Jin, S. Zhang, C. Wang and W. Zhang, *Biosens. Bioelectron.*, 2012, **32**, 224–230.
37 S. M. Taghdisi, N. M. Danesh, M. A. Nameghi, M. Ramezani, M. Alibolandi, M. Hassanzadeh-Khayat, A. S. Emrani and K. Abnous, *Biosens. Bioelectron.*, 2019, **123**, 14–18.
38 Q. Xu, S. Evetts, M. Hu, K. Talbot, R. Wade-Martins and J. J. Davis, *RSC Adv.*, 2014, **102**, 58773–58777.
39 X. You, S. C. Gopinath, T. Lakshmipriya and D. Li, *J. Anal. Methods Chem.*, 2019, **2019**, 6526850.
40 M. E. van Raaij, I. M. J. Segers-Nolten and V. Subramaniam, *Biophys. J.*, 2006, **91**, L96–L98.
41 C. N. Pace, F. Vajdos, L. Fee, G. Grimsley and T. Gray, *Protein Sci.*, 1995, **4**, 2411–2423.
42 Y. Zhang, M. Li, Q. Niu, P. Gao, G. Zhang, C. Dong and S. Shuang, *Talanta*, 2017, **171**, 143–151.
43 W. Lan, Q. Tan, J. Qiao, G. Shen and L. Qi, *Chin. Chem. Lett.*, 2019, **30**, 1627–1630.
44 S. Boyapalle, T. Wong, J. Garay, M. Teng, H. San Juan-Vergara, S. Mohapatra and S. Mohapatra, *PLoS One*, 2012, **7**, e29386.